ACS Catalysis

pubs.acs.org/acscatalysis Research Article

Structural Rearrangement in LSM Perovskites for Enhanced Syngas Production via Solar Thermochemical Redox Cycles

Asim Riaz, Takuya Tsuzuki, Felipe Kremer, Suchinda Sattayaporn, Muhammad Umair Ali, Wojciech Lipiński,* and Adrian Lowe*

Cite This: *ACS Catal.* 2020, 10, 8263−8276 Read Online

ACCESS | Metrics & More | Article Recommendations | Supporting Information

ABSTRACT: Oxygen carriers undergo many physiochemical changes such as particle growth and phase transformation during thermochemical redox reactions aimed at synthesizing solar fuels. In suitable materials, these changes favor the cyclic production of synthesis gas. Advanced study of these properties is of prime importance when strengthening the material selection criteria for thermochemical applications. Considering this, we investigate the redox behavior of $La_xSr_{1-x}MnO_3$ (LSM) perovskite oxide systems during dry and steam chemical looping reforming of methane. The durability and structural stability are studied for cyclic regeneration to the parent perovskite structure. It is observed that lanthanum addition suppresses the LSM structural disintegration during the reduction reaction and promotes its regeneration upon reoxidation. High syngas yields of up to 2.7 mmol g^{-1} are produced with 25% lanthanum content during 30 consecutive cycles of dry reforming of methane. H_2 purity is also increased by up to 18% in lanthanum-rich LSM structures when compared to pure $SrMnO_3$ with ∼74% H_2 purity. It is found that despite structural disintegration, manganese plays an active role in redox activities and its oxidation state is greatly influenced by lanthanum concentration and oxidation medium. We think that this study will supplement the in-depth investigation of the material's physiochemical properties before and after the redox reactions prior to selection of a suitable oxygen carrier/catalyst.

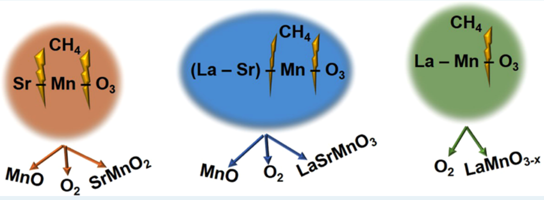

KEYWORDS: *perovskites, solar energy, thermochemical, syngas, structural disintegration—regeneration*

1. INTRODUCTION

Recent developments in solar fuel production technologies promise a smooth transition from fossil fuel to sustainable fuels for our future energy supply.[1,2] Solar fuels are produced by converting concentrated solar energy into chemical energy via thermochemical CO_2- and H_2O-splitting cycles. Syngas (a mixture of H_2 and CO) can be produced from methane reforming at relatively lower temperatures (900 °C) as compared to the thermal reduction reactions operated at temperatures as high as 1600 °C.[3−8] The chemical looping methane reforming cycles are completed in two steps in the presence of oxygen carriers or catalysts: (1) partial oxidation of methane, which results in the reduction of oxygen carriers, and (2) reoxidation of the reduced oxygen carriers by H_2O and CO_2, resulting in H_2 and CO, respectively.[9−11]

For efficient fuel production, the oxygen carriers must possess certain physiochemical properties such as structural and phase stabilities, high oxygen-exchange capacity, durability, high conversion efficiencies, and high fuel selectivity.[12−15] Cost-effectiveness of the oxygen-carrier material is another important factor that affects the overall fuel price.[13,15,16] In the past, an extensive amount of thermodynamic and experimental work has been conducted to identify suitable oxygen carriers. The most investigated materials include the oxides of Fe,[17−20] Zr,[21−25] Cu,[19,26,27] Ni,[21,26] Mn,[28−30] Ce,[13,15,31−35] and their derivatives. However, they still face significant challenges in commercial applications, e.g., high cost and severe agglomeration issues of Cu-based oxides, low reactivities of Mn-based oxides, toxicity of Ni, low selectivity and high sintering of Fe-based oxides, and limited oxygen-exchange capacity of Ce oxides.[31,36] Hence, for the commercial success of solar fuel production, there is a strong need to develop new oxygen-carrier materials.

Recently, perovskite oxides have gained substantial recognition as active oxygen-carrier materials for solar fuel production.[1,8,36−43] Perovskites have the general chemical formula of ABO_3, where "A" represents a rare-earth or alkaline-earth metal and "B" represents the transition metals.[44] Currently, over 250 types of perovskites have been experimentally synthesized and tested for numerous applications.[45] The flexibility to alter the composition of perovskites is advantageous over other metal oxides. For instance, the redox properties and oxygen vacancies can be tuned by the

Received: June 2, 2020
Revised: June 25, 2020
Published: June 26, 2020

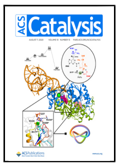

https://dx.doi.org/10.1021/acscatal.0c02439
ACS Catal. 2020, 10, 8263−8276

substitution/replacement of site A or B cations in their crystal structure. Typically, the B-site dopant is a lattice oxygen carrier in the perovskite structure, while the A-site elements indirectly influence the reactivity of perovskite by affecting the oxygen vacancies and valance states of B-site metal. For instance, partial substitution of lanthanum (La) with Sr in $LaFeCoO_6$ induces Fe/Co disorder and in turn generates oxygen vacancies in the lattice, resulting in higher cationic oxidation states.[36] Another study showed that partial substitution of La enhances the oxygen exchange in some perovskites that contain Mn−Fe and Co−Fe.[46]

Phase stability is a significant issue in perovskites for the partial oxidation of methane, as it determines the extent of solar fuel production efficiency. For example, Galinsky et al. reported that Mn-based perovskites show unstable behavior and irreversibly transform into spinel and Ruddlesden−Popper structures during chemical reforming of methane.[47] However, such structural instability issues are not observed upon nonstoichiometric oxygen exchange during inert reduction of metal oxides.[14] It is still not understood how deteriorative such structural decomposition of perovskite is toward the overall fuel production efficiencies and how structural stability can be achieved in perovskites during the cyclic redox reactions.

To address this research gap, an in-depth material-based study is carried out in this work using the $La_xSr_{1-x}MnO_3$ (LSM) perovskite. We investigated (1) the effect of the La/Sr ratio on phase stability and fuel production efficiencies, (2) the effect of methane partial oxidation (MPO) on the surface oxygen and cationic species of LSM and its relation to fuel production efficiencies, and (3) the effect of oxidation medium (CO_2 and H_2O) on the regeneration of perovskites with a detailed phase analysis and (4) we carried out morphological and chemical studies of LSM perovskite before and after redox cycles. $La_xSr_{1-x}MnO_3$ materials are synthesized using the electrospinning method. Their oxidation states, oxygen vacancies, phases, morphology, and chemical composition before and after redox cycles are studied. Isothermal redox reactions are carried out at 900 °C for 10 consecutive cycles.

It was found that, as an oxidizing medium, CO_2 induced more structural decomposition in LSM perovskites than H_2O. However, CO_2 as an oxidizing medium caused the formation of strontium carbonates and, as a result, decreases the carbon deposition on the perovskite, compared to H_2O. Although H_2O induced less structural instability in LSM than CO_2, it decreased fuel production efficiencies. La-rich LSM showed higher phase stability than Sr-rich LSM.

2. EXPERIMENTAL PROCEDURE

2.1. Materials and Methods.

Lanthanum chloride heptahydrate (Sigma), strontium carbonate (Sigma), and manganese(II) acetate tetrahydrate (Ajax Finechem) are used to synthesize the $La_xSr_{1-x}MnO_3$ perovskite. Polyvinyl pyrrolidone (PVP, Sigma, $M_w = 1.6 \times 10^6$) is used as the fiber-forming agent. Deionized (DI) water, ethanol (Ajax Finechem, absolute), and acetic acid (Ajax finechem) are used as solvents.

The perovskites are synthesized using the electrospinning technique, reported in our previous work.[14] The electrospinning technique has been utilized for material synthesis because it offers controllable fiber size. The reported studies suggested the electrospinning technique as simple, cost-effective, and suitable for an upscale synthesis of fibrous structures.[48,49] Briefly, the precursor materials are separately dissolved in a mixture of DI water, ethanol, and acetic acid. The solutions are then mixed along with PVP (molar ratio of 1:10 to the precursor materials) and stirred for 5 h to achieve a homogeneous sol and subsequently transferred to a syringe. Electrospinning of the perovskite is carried out at an accelerating voltage of 25 kV, a needle-to-collector distance of 15 cm, and a feed rate of 0.5 mL h^{-1}. A Cu plate wrapped with an Al foil is used to collect the as-spun fibers. Calcination of fibers is carried out at 1000 °C for 5 h at a ramp rate of 5 °C min^{-1}.

$La_xSr_{1-x}MnO_3$ with various La/Sr ratios (x = 0, 0.25, 0.50, 0.75, and 1.00) are produced. Hereafter, the samples are denoted according to the La/Sr ratio: SMO for x = 0, LSM25 for x = 0.25, LSM50 for x = 0.50, LSM75 for x = 0.75, and LMO for x = 1.00.

2.2. Material Characterization.

All samples are characterized before and after the redox cycles. Their morphologies are studied under an Ultra plus field emission scanning electron microscope (FESEM, Zeiss, Germany). A JEOL-2100F high-resolution transmission electron microscope (HR-TEM, JEOL, Japan) is utilized to investigate the particle size distribution, lattice plane spacing, and particle morphology. For TEM studies, a drop of powder suspension in ethanol is placed onto a lacey carbon-coated 200 mesh Cu grid. The primary image processing, the measurements of lattice plane spacing, and particle size analysis are carried out using ImageJ image processing software. Energy-dispersive X-ray spectroscopy (EDS) elemental maps are acquired in scanning transmission electron microscopy (STEM) mode using the HR-TEM.

Information about the surface and porosity of the LSM powders was obtained via the Brunauer−Emmett−Teller (BET) technique using TriStar II, Micromeritics. Samples were prepared by degassing at 180 °C under a vacuum (0.1 mbar) atmosphere for 4h, while nitrogen adsorption−desorption isotherms were acquired at 7 K.

Powder X-ray diffraction (PXRD) analysis is conducted using a D2 phaser diffractometer (Bruker) equipped with a Cu Kα (1.54 Å) radiation source operating at 300 kV voltage and 10 mA current. XRD patterns are acquired at a scan rate of 0.75° min^{-1} in the diffraction angle range of 10−80° with an increment step of 0.02°. For the phase quantification of LSM powders, Match version 3.8.1.143 software (Crystal Impact, Germany) is utilized to apply the Rietveld refinement technique on the acquired XRD spectra.

An ESCALAB 250 Xi X-ray photoelectron spectrometer (XPS, Thermo Fisher) is utilized for the chemical analysis of LSM powder surfaces. The microprobe consists of a 180° double-focusing hemispherical analyzer. An aluminum Kα radiation source with a spot size of 200−900 μm is operated at 15 kV voltage and a current of 12 mA. Spectra are obtained at different spots on a sample mount with an area of 5 × 5 mm and a depth of 4 mm. Scanning is carried out with an energy of 160 eV for survey spectra and 40 eV for high-resolution spectra. The acquired spectra are deconvoluted using CasaXPS processing software version 2.3.18 (Casa Software, U.K.). Binding energies obtained in the survey spectra are compared with the reference Carbon C 1s peak at 284.8 eV.

Synchrotron X-ray measurements are carried out at the Synchrotron Light Research Institute (SLRI), Thailand. The synchrotron radiation source is generated at the storage ring with a beam energy of 1.2 GeV. The beam current has a range of 80−150 mA, with a maximum photon flux of $1.1{-}1.7 \times 10^{11}$ photons.s^{-1}. X-ray absorption near-edge spectra (XANES) and

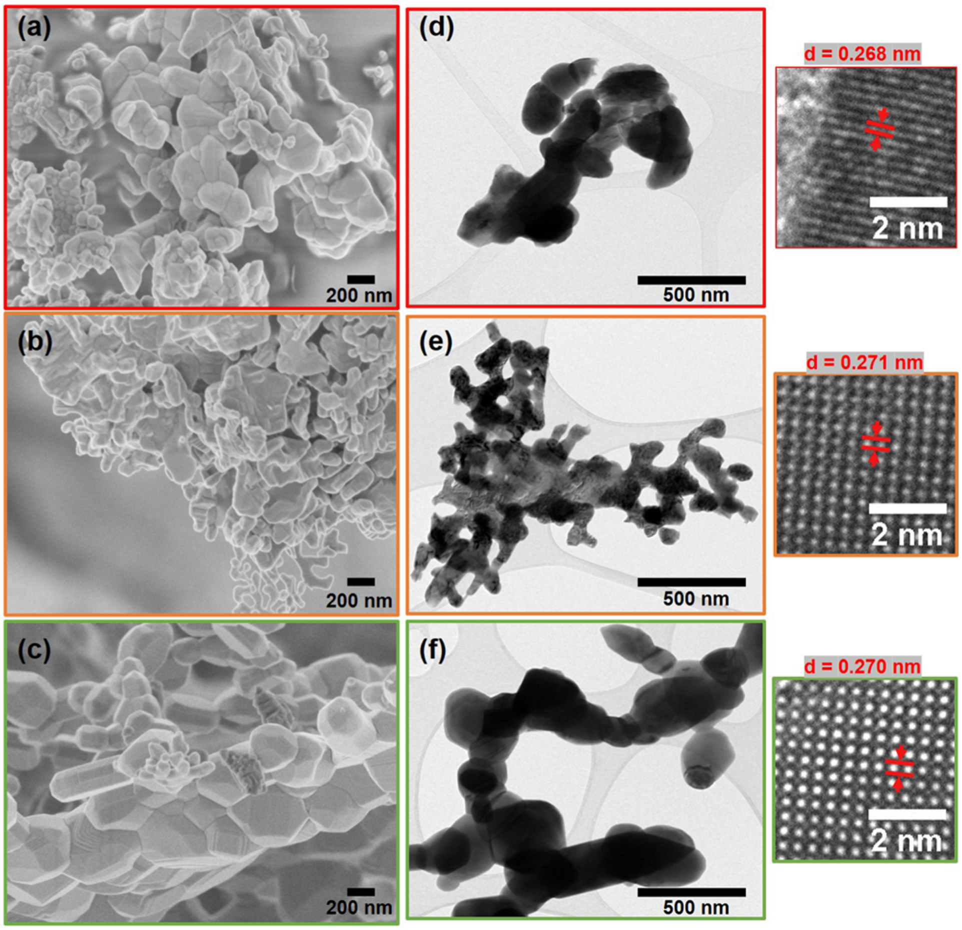

Figure 1. Morphological representation of as-prepared LSM perovskite powders: FESEM micrographs of (a) SMO, (b) LSM50, and (c) LMO powders. TEM images of (d) SMO, (e) LSM50, and (f) LMO powders. HR-TEM images show the inner planner spacing of respective SMO, LSM50, and LMO samples.

extended X-ray absorption fine structure (EXAFS) of the Mn K-edge are acquired at the SUT-NANOTEC-SLRI XAS beamline (BL5.2). A rectangular frame with a groove (3 × 10 mm) is utilized to hold the powder samples with a Kapton sticky tape to allow X-ray transmission. Standard Mn foil, MnO, Mn_2O_3, Mn_3O_4, and MnO_2 samples are also analyzed to compare and elucidate the oxidation states of experimental samples. Athena analysis software is utilized to process the XANES and EXAFS data.

2.3. Thermochemical Cycle Test. Thermogravimetric analysis (TGA) and differential thermal analysis (DTA) are carried out using a NETZSCH STA 449 F3 Jupiter. Mass change during three consecutive redox cycles is recorded as an indication of active redox reactions. The cyclability of LSM powders is investigated by performing 30 consecutive redox cycles. Powder samples are reduced and then reoxidized under a 10 mL min^{-1} flow of CH_4 and CO_2, respectively. The total gas flow is kept constant at 125 mL min^{-1}, balanced with Ar carrier gas. Ar (125 mL min^{-1}) is used after every reduction and oxidation reaction to purge or sweep any byproducts and reacting gases from the system. Approximately 40 mg of powder is heated to 900 °C with a ramp rate of 20 °C min^{-1}. Isothermal reduction and oxidation reactions are carried out for 20 and 10 min, respectively, while the Ar gas sweeping step is set for 5 min.

Another experimental setup is used to record the instantaneous gas evolution during redox reactions. A high-grade alumina tube is placed axially in the center of an infrared gold image furnace (P4C-VHT, Advance Riko, Japan). A 2 mm thick layer of high-temperature-resistant Al_2O_3−SiO_2 (Al_2O_3 97 and 3% SiO_2, ZIRCAR) fibers is placed in the middle of the tube to support ∼250 mg of a powder sample. Another fiber layer is placed right above the sample while keeping 2−3 mm from it, to ensure an easy solid−gas transfer. Gas flow controllers (F201CV, Bronkhorst) are used to regulate the flow rates and the pneumatically actuated valves (1315R, Swagelok) are operated by an in-house-developed LabVIEW (National Instrumental) program code. A B-type thermocouple sealed in an alumina sheath is used to monitor the sample temperature. The product gas composition is acquired by a quadrupole mass spectrometer (OmniStar GSD 320, Pfeiffer Vacuum).

In the infrared furnace, samples are heated at 900 °C with a ramp rate of 100 °C min^{-1} under a 500 mL min^{-1} Ar flow. Reduction of the sample is carried out for 20 min under a 20 mL min^{-1} CH_4 flow and then the samples are reoxidized under a 10 mL min^{-1} CO_2 gas flow for 10 min. The total gas flow rate during the reduction−oxidation reactions is kept constant at 250 mL min^{-1}, balancing with the Ar as a carrier gas. A 5 min sweeping step is introduced before and after every reduction−oxidation reaction with an Ar 500 mL min^{-1} flow to remove

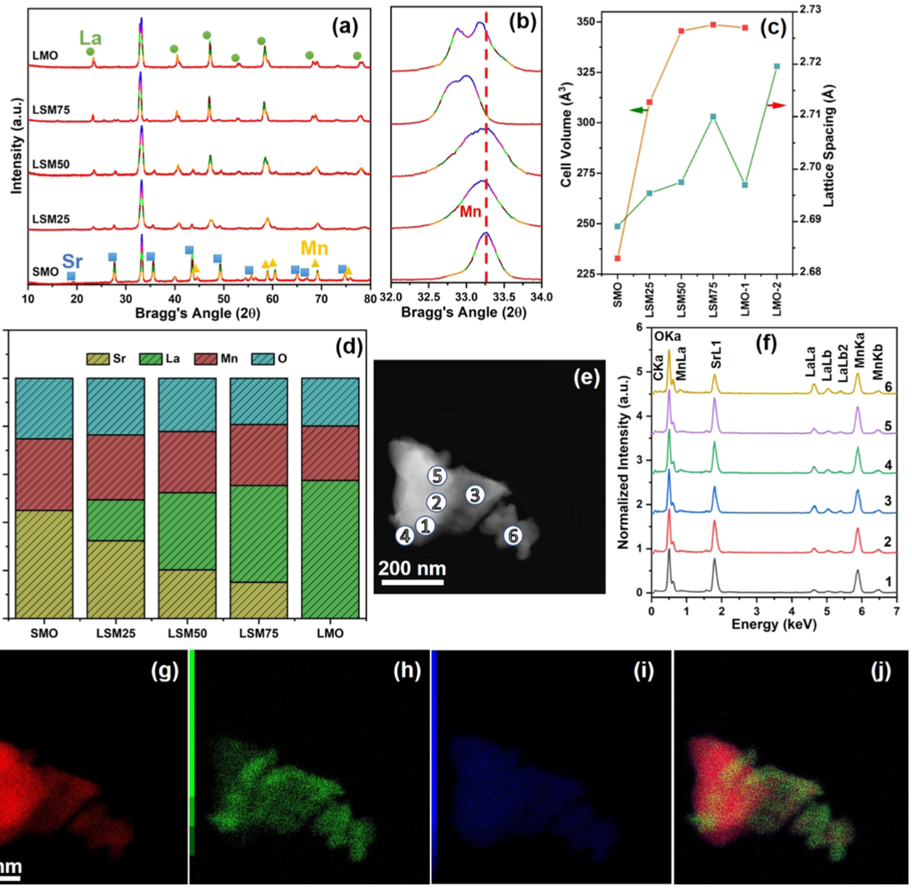

Figure 2. Structural and chemical analyses of as-prepared LSM perovskites: (a) XRD patterns presenting the phase evolution with different La concentrations. (b) Shift and split of manganese oxide Bragg's angle peak with lanthanum incorporation from 0 to 100%. (c) Cell volume expansion and Bragg's angle peak shift in LSM structures due to large lanthanum cations. (d) Effect of lanthanum addition on elemental distribution in LSM Perovskites. (e) Grayscale STEM image of the pristine LSM25 sample corresponding to (f) EDS spectra measured at six different points. STEM–EDS colored maps of (g) Sr, (h) La, (i) Mn, and (j) overlay of pristine LSM25 powder samples.

any remaining reactants and product gases before starting a new cycle. For water-splitting reactions, steam vapor is generated from DI water at 95 °C in a bubbler. An Ar flow of 30 mL min^{-1} is used to carry the steam vapor, which is further diluted with a 220 mL min^{-1} Ar flow before it reaches the reactor.

3. RESULTS

3.1. LSM Perovskites Before Redox Cycles.

The morphological investigations of the as-prepared LSM perovskite powders revealed clusters of small particles in Sr-rich samples, while La-rich powders contained an ordered structure. In addition, high lanthanum contents increased the particle size, as shown in Figure 1a−c. HR-TEM images of as-prepared LSM powders complemented the FESEM findings on the increase in particle size and lattice planner spacing in La-rich LSM powders, as shown in Figure 1d−f. Pure SMO has an average particle size of 115 ± 8 nm, which increased to 151 ± 18 nm with 50% addition of lanthanum, while the pure LMO particles are the largest, with an average size of 310 ± 25 nm. The lattice planner spacing increased from 0.268 nm for pure SMO to 0.271 nm in LSM50 and 0.270 mm in pure LMO.

The XRD patterns of as-prepared samples are shown in Figure 2a. Addition of lanthanum in SMO induced a structural change. As the amount of La increases, the Mn−O (111) peak around $2\theta = 34°$ shifts to lower angles. High lanthanum contents induce strains in the Mn−O lattice, which can be observed as diffraction peak splits in XRD patterns of LSM materials with 50% or more lanthanum (Figure 2b). For instance, the split of the Mn−O peak at around 34° is a result of diffraction from (110) and (104) planes in pure LMO samples. Accordingly, the cell volume increased from 232 Å^3 for SMO to 346 Å^3 for LSM50. By the same token, inner lattice spacing increases with La addition (Figure 2c).

The Rietveld refinement on the XRD patterns (Table SI-1) revealed that the SMO powder contains the 100% $SrMnO_3$ phase (COD # 96-152-9599), which decreased to 13.8% with the addition of 25% La. On the other hand, 50 and 75% La additions result in 94.3% $La_{0.6}Sr_{0.4}MnO_3$ (COD #96-153-3289) and 91.5% $La_{0.7}Sr_{0.3}MnO_3$ (COD #96-152-1157) phases, respectively. The remaining phase in LSM50 and LSM75 is the $LaMnO_3$ (COD #96-153-1527) phase. However, it can be inferred that Sr has a stronger tendency than La to form a tertiary oxide with Mn, while higher lanthanum content supports the development of the $LaSrMnO_3$ structure.

The STEM study revealed that Sr and Mn are homogeneously distributed in SMO (Figure SI-1). However, addition of lanthanum resulted in various Sr- and La-rich regions due to the formation of segregated phases, as discussed in the XRD analysis of as-prepared LSM powders. As an example, Figure 2g−j show the elemental maps of the as-prepared LSM25 powder, while Figure 2f shows the change in the La energy

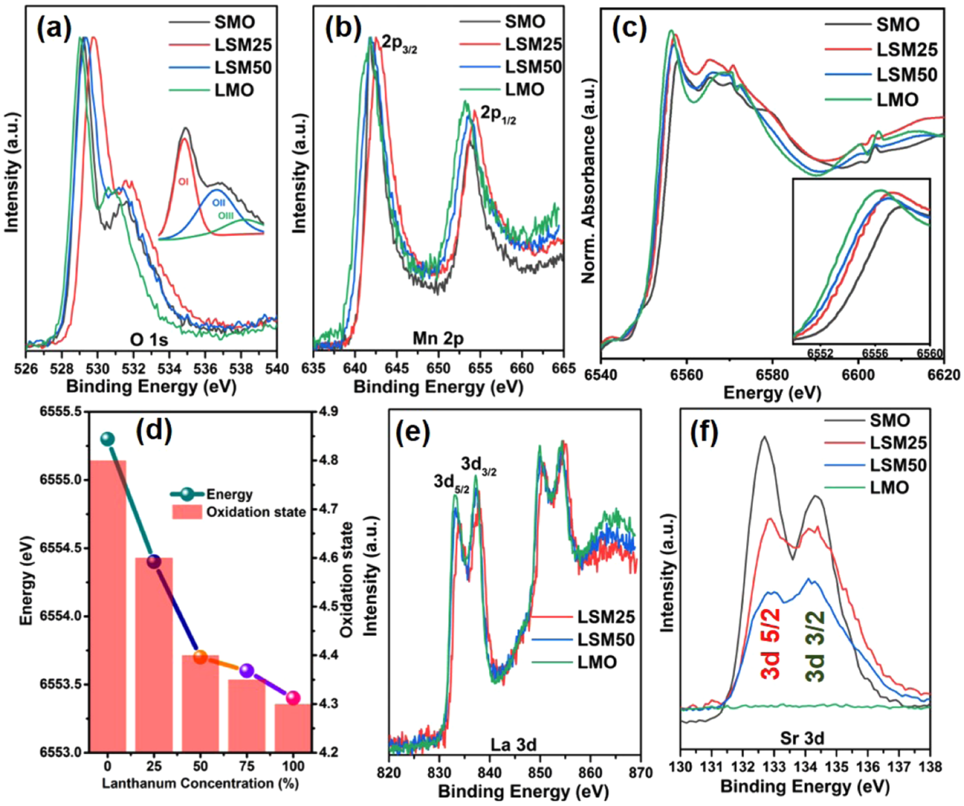

Figure 3. Surface and bulk chemical analyses of pristine LSM structures with variable La concentrations: XPS spectra representing (a) oxygen, O1s; (b) manganese, Mn 2p species. Shifts in binding energies and changes in peak intensity describe the change in the chemical state of the LSM structure. (c) Mn K-edge XANES spectra of pristine LSM powders showing variations in the photon energies with lanthanum addition. (d) Photon energy shift and change in the oxidation state as a function of the lanthanum concentration are presented. The data for the oxidation state is obtained from XANES analysis. XPS spectra of (e) lanthanum, La 3d; and (f) strontium, Sr 3d, species on pristine LSM powder surfaces.

counts at different spots of the gray image shown in Figure 2e. Figure 2d shows the elemental compositions determined from STEM−EDS spectra, where large La cations induced oxygen vacancies in La-rich LSM. The EDS elemental concentration data drifts from the stoichiometric elemental calculations by only 9 ± 2%.

The XPS results of as-synthesized LSM powders are shown in Figure 3a,b. The O 1s peak of all LSM structures lies around 529.3 eV, with no significant energy shift with the amount of La (Figure 3a). The neighboring shoulder at around 531.15 eV represents the presence of oxygen species due to possible surface oxidation or advantageous contaminants (CO_2, moisture, etc.).[50] The Mn 2p peak has significantly split spin−orbit components 2p 1/2 (∼653 eV) and 2p 3/2 (∼642 eV) as shown in Figure 3b. The energy difference of the split (ΔBE) is 11.58 eV in SMO and decreases to 11.37 eV in LMO. This occurs due to the shift of Mn 2p 1/2 and Mn 2p 3/2 peaks toward lower binding energies, representing a change in Mn oxidation states as a function of the La concentration. The variation in the ratio between the intensities of Mn 2p 3/2 and 2p 1/2 peaks also indicates the change in the electronic configuration of Mn. Generally, Sr-rich LSM powders show a higher 2p 3/2 to 2p 1/2 ratio than La-rich LSM powders. The increase in the intensity of the 2p 1/2 peak is indicative of smaller cationic charge on Mn in La-rich LSM structures.[14] The Mn 2p 3/2 peak at binding energies of greater than 642 eV represents the +4 oxidation state of Mn. Nevertheless, the approximate oxidation state can be calculated from the splits of the Mn 3S peak.[51] The split of Mn 3s peaks increases from 3.9 to 5.32 eV with La addition and reaches a maximum in LSM75. The ionic charge on Mn is approximately +4, the highest in SMO, which decreases to +3.7 in LMO.

XANES analysis provides useful information about the oxidation states and oxygen vacancies in LSM samples. Mn K-edge XANES spectra are presented in Figure 3c. The Mn K-edge shifts monotonically to lower photon energies as a function of the La concentration. The edge energy of SMO is 6555.3 eV, which decreases to 6553.4 eV in LMO. Mn oxidation states can be calculated from the Mn K-edge spectra and by comparing to the Mn K-edge spectra of MnO, MnO_2, and Mn_2O_3 standard samples. As shown in Figure 3d, addition of La lowers the oxidation state from approximately +4.0 for SMO to +3.6 for LMO.

The charge shift on Mn greatly affects the oxygen vacancies present in the LSM structure; a higher Mn oxidation state represents a higher number of oxygen vacancies. The results of XPS and XANES studies indicate that oxygen vacancies can be controlled in the LSM structures by changing the La concentration.

The energy difference in the satellite (S) and main (M) XPS peaks of La $3d_{5/2}$ and La $3d_{3/2}$ (ΔBE) with La addition indicates the change in the chemical state of surface La species. As shown in Figure 3e, a higher La content shifts the La 3d 5/2 peak to a higher binding energy: the ΔBE increased from 3.67 eV in LSM25 to 4.22 eV in LSM50. This indicates that the chemical bonds around La ions are stronger in La-rich samples, which would contribute to inhibiting the structural deterioration of LSM samples by methane and to facilitating a

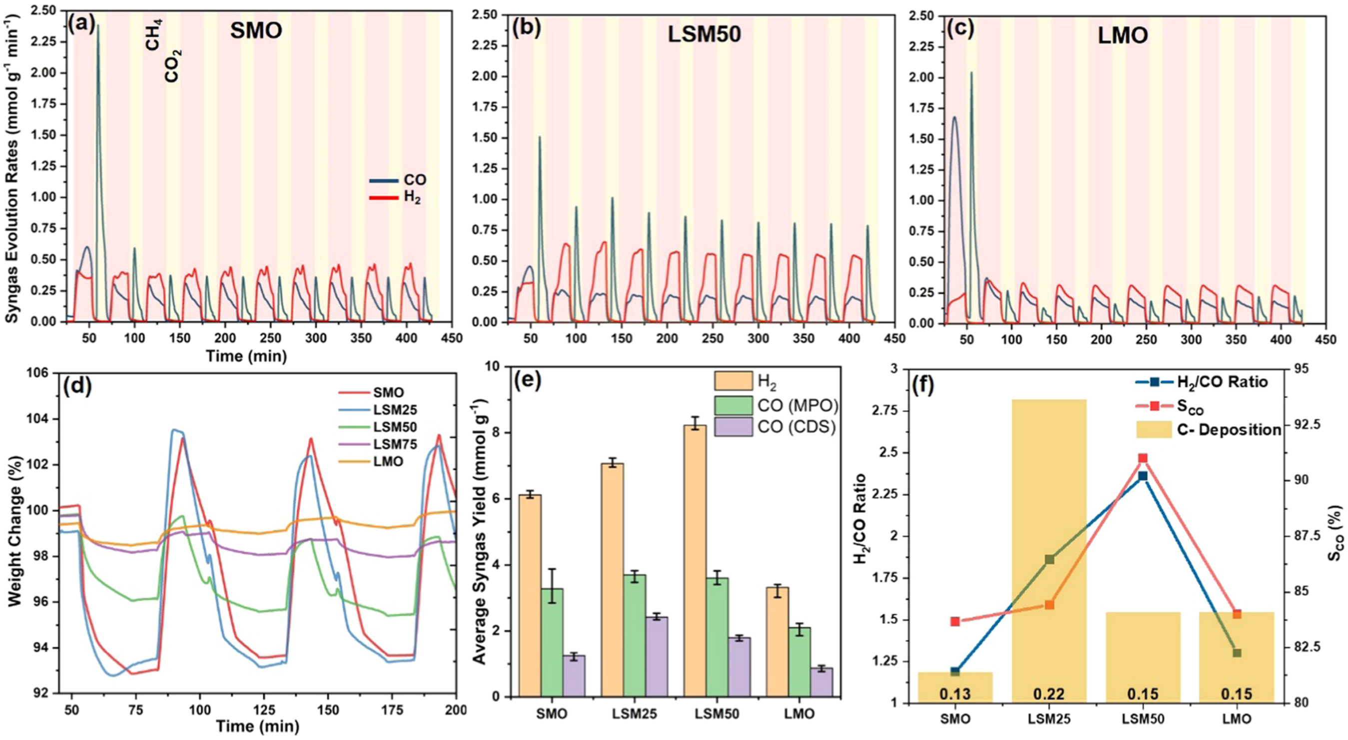

Figure 4. Thermochemical redox performance of LSM perovskites for MPO−CDS cycling: syngas production rates by (a) SMO, (b) LSM50, and (c) LMO samples. (d) TGA−DTA analysis of LSM perovskites for MPO−CDS cycles in terms of mass change during redox reactions. (e) Average syngas yield in reduction and oxidation reactions during MPO−CDS cycles. (f) Carbon deposition, CO selectivity, and H_2/CO ratios presented as a function of lanthanum concentration. MPO reaction rate data is utilized to calculate mmol of deposited carbon and H_2/CO ratios. Both reduction and oxidation reaction rate data are utilized to calculate CO selectivity.

nonstoichiometric reduction, which will be discussed later. Figure 3f shows an orbital split of the Sr 3d peak into 3d 3/2 and 3d 5/2 peaks at around 134.4 and 132.5 eV, respectively. It is evident that the shape of this split is highly affected by the La concentration. The change in the peak shape is attributed to the rearrangement of the Sr electronic configuration instead of a change in the oxidation state of Sr.,[52]

3.2. Rate and Yield of Thermochemical Syngas Production 1: MPO−CDS Cycle.

The syngas production rates and yields, CO selectivity (S_{CO}), purity of H_2, and moles of deposited carbon were calculated by reactions 1−5.[53] The S_{CO} is defined as the ratio of CO yield to the sum of CO and CO_2 yields produced in the MPO step (Reaction 3). The deposited carbon refers to the moles of solid carbon produced and deposited onto the material's surfaces due to the thermal cracking of methane (Reaction 6).

$$\text{Syngas Rates} = \frac{(((\%\text{ gas} \div 100) \times \text{total gas flow}) \div 22400)}{\text{Mass or Moles of materials}} \quad (1)$$

$$\text{Syngas yield} = \text{Syngas production rates} \times \text{Total time for the reduction or oxidation step} \quad (2)$$

$$\text{CO Selectivity} = \frac{\text{CO yield in MPO step}}{(\text{CO} + \text{CO}_2)\text{ yields in MPO step}} \times 100 \quad (3)$$

$$\text{Purity of H}_2 = \frac{\text{H}_2\text{ yield in WS step}}{(\text{CO} + \text{H}_2)\text{ yields in WS step}} \quad (4)$$

$$\text{Deposited Carbon} = \frac{\text{yield in CDS step}}{(\text{H}_2 + \text{CO})\text{ yields in MPO step}} \quad (5)$$

$$CH_4 \rightarrow C + 2H_2 \quad (6)$$

Figure 4 shows the thermochemical redox performance of LSM perovskites for oxidation−reduction cycling. All LSM powders demonstrate stable syngas production rates during reduction and oxidation reactions. During methane partial oxidation (MPO) reactions, the syngas production rates of SMO were approximately 0.42 mmol_{H_2} g^{-1} min^{-1} and 0.30 mmol_{CO} g^{-1} min^{-1} (Figure 4a). La addition enhanced the production rates and maximum values of 0.60 mmol_{H2} g^{-1} min^{-1} and 0.25 mmol_{CO} g^{-1} min^{-1} were achieved with 50% La addition (Figure 4b). Further increase in La lowered the rates, while the pure LMO sample produced only 0.31 mmol_{H_2} g^{-1} min^{-1} and 0.21 mmol_{CO} g^{-1} min^{-1} (Figure 4c). Overall, the oxidation recovery in terms of CO production rates during the CO_2-splitting (CDS) reaction increased with La addition from 0.36 mmol_{CO} g^{-1} min^{-1} for SMO to 0.84 mmol_{CO} g^{-1} min^{-1} for LSM50.

TGA−DTA analysis is performed to replicate the MPO−CDS redox cycles in terms of mass change (Figure 4d). LSM25 showed the highest mass change of up to 11%, followed by SMO with 9.5% and then LSM50 with 4.5%. LSM75 and LMO show only negligible mass changes. Structural rearrangement in LSM materials during redox cycles results in larger amounts of oxygen release as compared to nonstoichiometric oxygen exchange in La-rich LSM materials, which results in greater

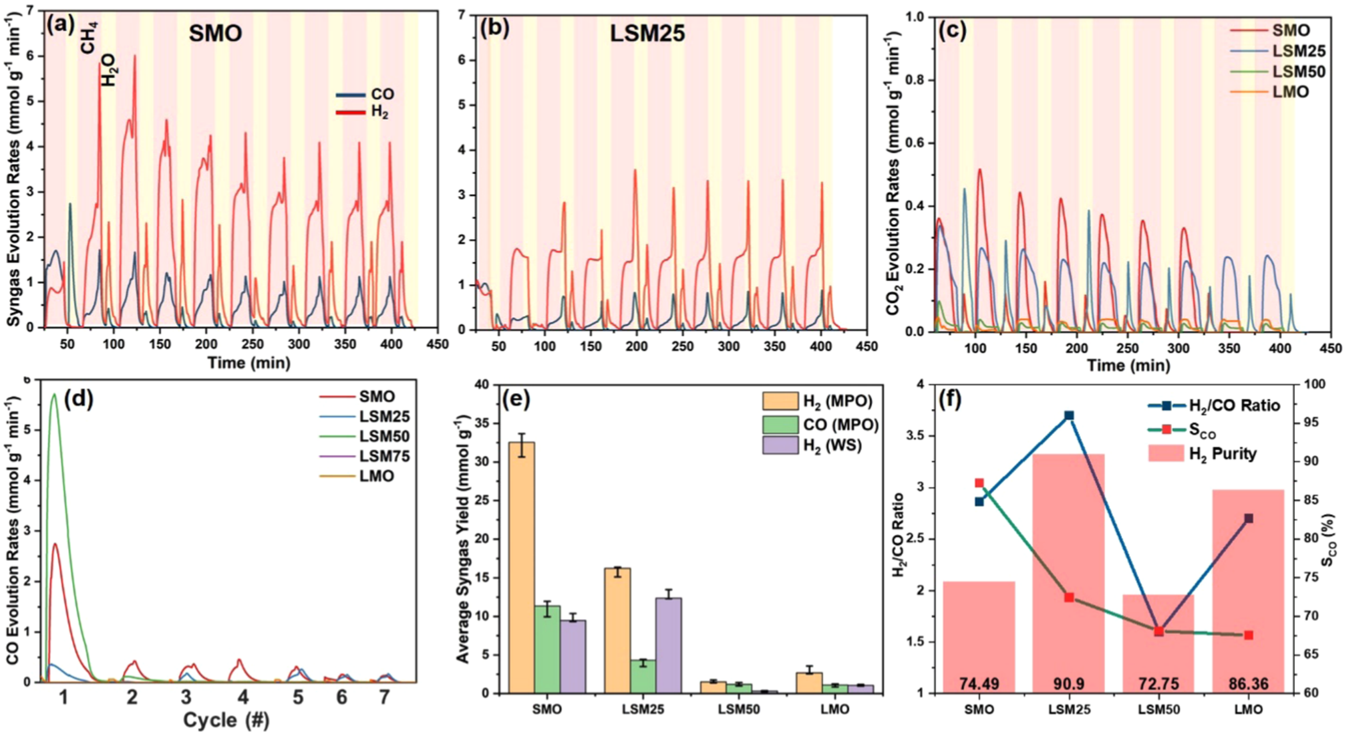

Figure 5. Thermochemical redox performance of LSM samples during MPO−WS cycles: syngas production rates from (a) SMO, (b) LSM25 samples, and (c) rates of CO_2 produced by LSM materials, during reduction and oxidation reactions of MPO−WS cycles. (d) CO evolution rates during the WS reaction by LSM powders with different lanthanum concentrations. (e) Average syngas yields from LSM powders during redox cycles. (f) H_2/CO ratios, CO selectivity, and H_2 purity achieved by different LSM powders. H_2 purity is calculated by the CO and H_2 rate data acquired during the WS reaction.

mass changes in Sr-rich LSM materials when compared to that of La-rich LSM.

Syngas production yields are calculated by taking the average of H_2 and CO produced during reduction and oxidation reactions of 10 consecutive cycles, as shown in Figure 4e. The syngas yield is the highest for LSM50, with average values of 8.23 $mmol_{H_2}$ g^{-1} and 3.61 $mmol_{CO}$ g^{-1}, followed by LSM25, with 7.07 $mmol_{H_2}$ g^{-1} and 3.72 $mmol_{CO}$ g^{-1}, while the pure LMO sample produced the lowest yields of 3.33 $mmol_{H_2}$ g^{-1} and 2.12 $mmol_{CO}$ g^{-1}.

Addition of La greatly influenced the reforming reaction in terms of H_2/CO ratios and CO selectivity; the H_2/CO ratio is increased from 1.18 for SMO to 2.36 for LSM50 (Figure 4f). CO selectivity increases with La addition and is the highest (ca. 91%) for LSM50, followed by LSM25, LMO, and SMO. Due to its high oxidation ability, LSM25 gives the highest CO yield of 2.42 $mmol_{CO}$ g^{-1}, followed by LSM50 with 1.80 $mmol_{CO}$ g^{-1} of CO, during the CO_2-splitting reaction, as shown in Figure 4e.

The role of carbon deposition in the CO yield is studied to estimate the actual oxygen recovery in the LSM structures. Moles of calculated carbon are the highest in LSM25, ca. 0.22 mmol, and the lowest (0.13 mmol) in SMO. Despite the higher amount of deposited carbon, LSM25 can be considered as the best LSM perovskite, where efficient carbon oxidation results in considerable CO and H_2 yields without affecting the H_2/CO ratio of 1.95. However, H_2/CO ratios close to 2 can be achieved by optimizing the CH_4/O_2 ratios (R). Studies have found that the $R = 1$ lowers the H_2 production rates, while producing large quantities of CO_2, whereas the H_2/CO ratios drastically increase due to the insufficient oxygen present to oxidize methane, when $R > 2$.[53]

3.3. Rate and Yield of Thermochemical Syngas Production 2: MPO−WS Cycle.

Water-splitting (WS) cycles were performed to study the oxidation behavior of the LSM structures with different La concentrations. In addition, the effects of La on H_2 purity and syngas yield were also studied. Syngas production rates from the SMO sample are the highest, with maximum values of 4.28 $mmol_{H_2}$ g^{-1} min^{-1} and 1.16 $mmol_{CO}$ g^{-1} min^{-1}, as shown in Figure 5a. LSM25 is the only LSM system with high rates of 3.13 $mmol_{H_2}$ g^{-1} min^{-1} and 0.85 $mmol_{CO}$ g^{-1} min^{-1} (Figure 5b), while LSM50, LSM75, and LMO have negligible production rates. The results indicate that the metal oxide species that are formed after reduction of the LSM perovskites are incompatible with steam to cause the reoxidation reaction. The reasons will be discussed in detail in the following sections around the structural study of LSM samples after redox cycles.

The syngas yields for SMO were the highest at 32.6 $mmol_{H_2}$ g^{-1} and 11.48 $mmol_{CO}$ g^{-1} during the MPO−WS cycles, as shown in Figure 5e. Considering the syngas yields and CO selectivity, SMO and LSM25 appear to be the best among the LSM samples, while they also produced considerable CO_2, with a maximum rate of 0.33 mmol g^{-1} min^{-1}, as shown in Figure 5c. In addition, the H_2/CO ratios for SMO and LSM25 are greater than 2, which indicates the formation of solid carbon (resulting from methane cracking) in addition to the H_2 and CO products during the ~~of~~ methane partial oxidation reaction. However, LSM25 produced a H_2 yield of 12.41 mmol g^{-1} (Figure 5e). The purity of H_2 produced with LSM25 is also

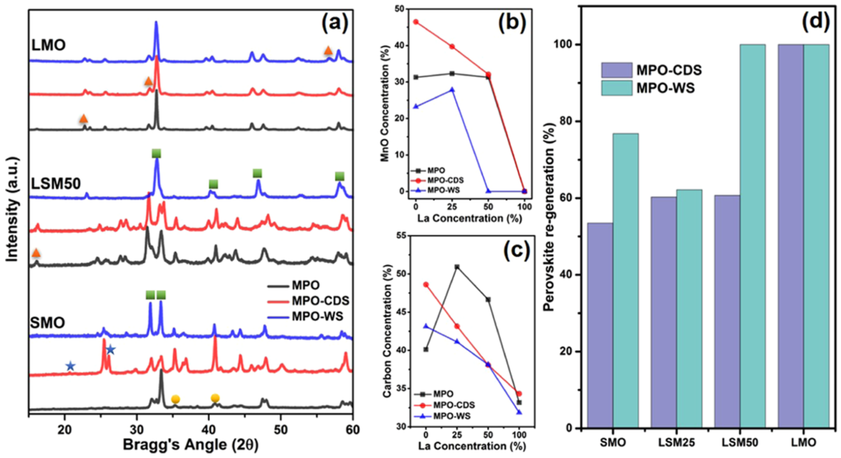

Figure 6. Bulk and surface chemical analyses of LSM perovskites after thermochemical redox cycles: (a) XRD patterns of SMO, LSM50, and LMO powders after MPO, MPO−CDS, and MPO−WS cycles representing regeneration of the LSM structure. Green squares represent the (La/Sr) MnO_x, yellow circles correspond to the MnO phase, while blue stars and orange triangles depict the presence of Sr and La, respectively. (b) Concentration of the MnO phase formed after reduction and reoxidation reactions in LSM structures with different lanthanum concentrations. XRD data is utilized to calculate the MnO phase by Rietveld refinement methods. (c) Carbon deposition on LSM powder surfaces as a function of lanthanum concentration. Carbon concentration is calculated from XPS data obtained in the C 1s region. (d) Perovskite regeneration in LSM structures during MPO−CDS and MPO−WS cycles. The regeneration is quantified from the concentration of the LSM structure formed after the reoxidation reaction by CO_2 and H_2O.

higher than that with SMO, where only 9.1% of CO is observed during the WS reaction, as shown in Figure 5f.

3.4. LSM Perovskites after CDS and WS Cycling.

Thermochemical performance can be understood by investigating the structural changes occurring in LSM structures during MPO, MPO−CDS, and MPO−WS reactions. Methane partial oxidation is the first step for all MPO−CDS and MPO−WS reactions, which explains the initial structural changes occurring in the LSM structure upon reduction. Next, the regeneration of the LSM structure upon reoxidation during the CO_2- and H_2O-splitting reactions determines the cyclability and durability of LSM oxygen carriers during the redox cycles. XRD is utilized to study the LSM structures after reduction and reoxidation reactions. XRD patterns of reduced LSMs with various La concentrations are presented in Figure 6a. The LSM structures go through a range of structural destructions during the MPO reaction. A prime product of LSM structural breakage is MnO, which is high in Sr-rich LSM structures and decreases with La addition. Table SI-2 presents the products formed after the redox reactions. SMO contains 7.7% Mn_2O_3, which is not observed in other LSM structures. In addition, $SrMnO_3$ transforms to Sr_2MnO_4, which is observed in reduced SMO and LSM25 samples. With 50% La, a higher fraction of $LSMO_{2.5}$ is obtained than Sr_2MnO_4 and MnO. No MnO or $SrMnO_3/Sr_2MnO_4$ is observed in LSM75 and LMO after reduction. This clearly indicates the nonstoichiometric reduction of LSM75 and LMO, where La prevents structural deterioration. In contrast, the reduction of Sr-rich LSM structures leads to breakage and results in various segregated phases.

Elemental segregation was visualized by analyzing reduced LSM samples with STEM−EDS mapping. Figure SI-2a−e represents the STEM maps of Sr, Mn, and La elements in the reduced LSM25 sample. Regions with high concentrations of Mn, La, and Sr can be observed in the overlay image of individual elemental maps, consistent with the results of the XRD study.

The reoxidation behavior of reduced LSM species via CO_2- and H_2O-splitting reactions was studied in terms of structural changes and was correlated to syngas production performance. Figure 6a shows the XRD patterns of LSM samples obtained after 10 consecutive MPO−CDS and MPO−WS cycles. The recovery of the $SrMnO_3$ phase is observed along with an increase in the MnO phase by 8% in SMO. The MnO phase is the highest in SMO after MPO−CDS cycles. An increase in the MnO phase suggests continuous breakage of LSM structures after successive reduction−oxidation reactions, resulting in the irreversible formation of the MnO phase. This also indicates that the MnO phase does not play any role in the fuel production step of CDS and WS cycles. The formation of the MnO phase drastically decreases by 17% with 50% of La addition, while no MnO phase is observed in LSM75 and LMO after 10 MPO−CDS cycles (Figure 6b). This also explains the higher extent of recovery of the LSM phase and inhibition of structural breakage during the MPO reaction in La-rich LSM structures.

XRD analysis of the reoxidized LSM samples reveals interesting information and explains the low-end fuel production performance of some LSM perovskites during MPO−WS cycles. As anticipated, structural breakdown was prominent in the strontium-rich LSM structures, resulting in the highest amounts of up to 37.9% of the MnO phase in LSM25, followed by 23.2% in the pure SMO powders. However, MnO is not present in LSM50, LSM75, and LMO after WS reactions. Perovskite regeneration percentage can be calculated from the phase quantification of XRD patterns (Table SI-2), as shown in Figure 6d. LSM50 and LMO showed 100% regeneration of the perovskite structures after oxidation by steam. However, Sr-rich LSM powders contain approximately 60% of the LSM perovskite phase and the rest is the MnO phase after MPO−WS cycling. The recovery of original perovskite phases is increased in all LSM structures by 16−25% during MPO−WS cycles as compared to that of MPO−CDS cycles. This is possible due to suppressed LSM breakage and formation of the MnO phase during MPO−WS cycles.

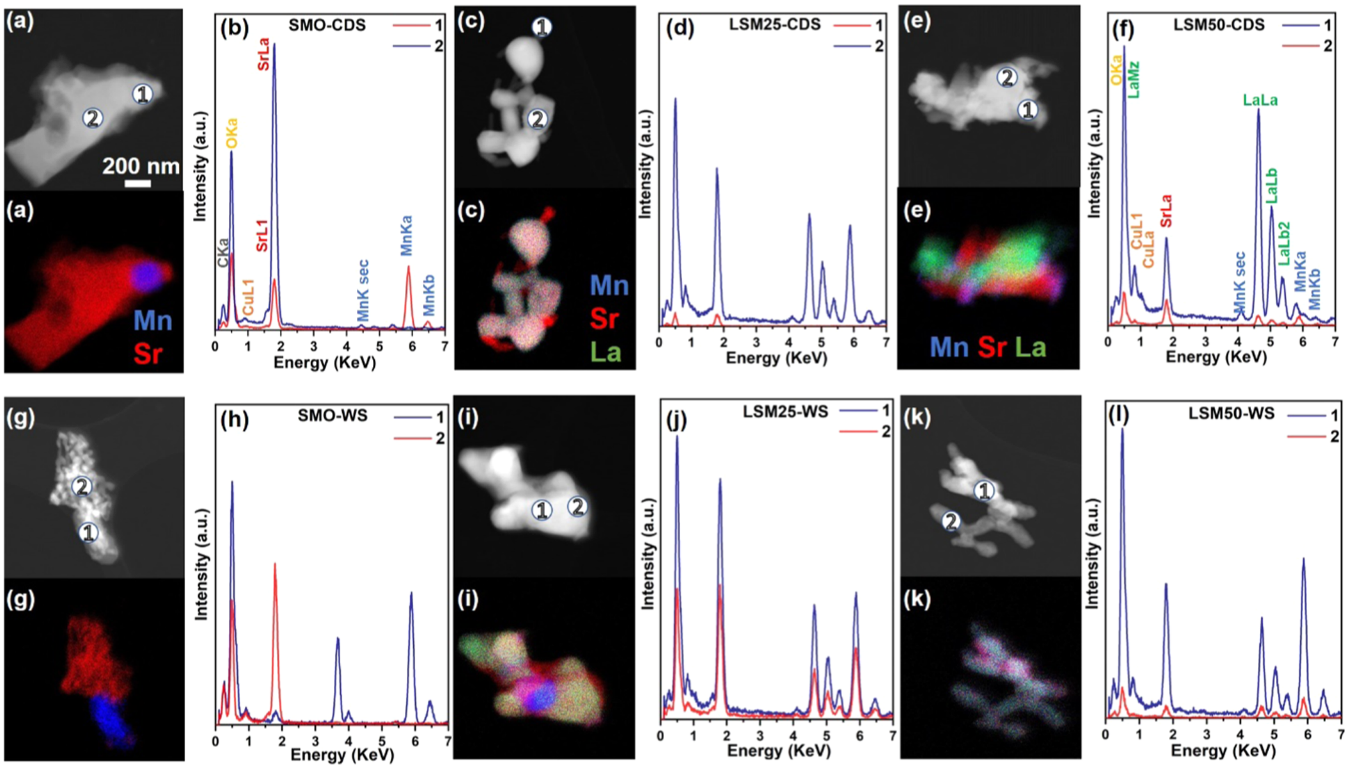

Figure 7. Chemical analysis of SMO, LSM25, and LSM50 samples after MPO−CDS and MPO−WS cycling carried out by STEM−EDS analysis: grayscale and overlay color maps of (a) SMO, (c) LSM25, and (e) LSM50 samples after MPO−CDS and (g) SMO, (i) LSM25, and (k) LSM50 samples after MPO−WS cycling. STEM−EDS spectra of (b) SMO, (d) LSM25, and (f) LSM50 correspond to MPO−CDS cycling and (h) SMO, (j) LSM25, and (l) LSM50 refer to MPO−WS cycling. Red, blue, and green colors show Sr, Mn, and La, respectively, while purple, yellow, and pink colors are the overlay effects of red, blue, and green colors.

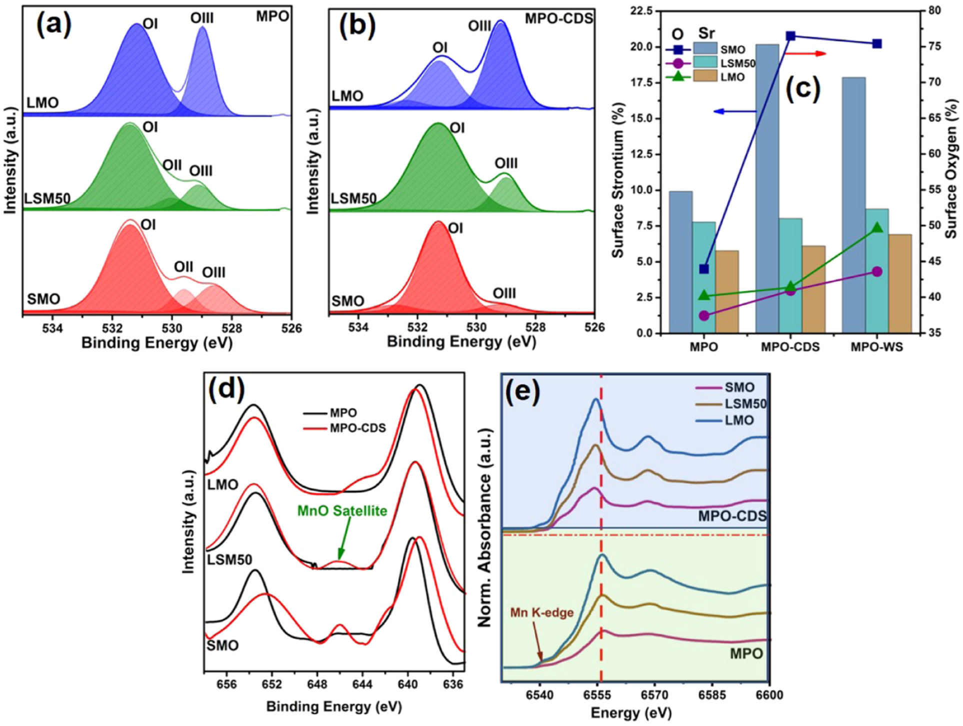

Figure 8. Surface and bulk chemical analyses after redox cycling: (a) XPS O 1s spectra of (a) reduced and (b) MPO−CDS-cycled SMO, LSM50, and LMO samples. (c) Relation of surface strontium with surface oxygen species on MPO-, MPO−CDS-, and MPO−WS-cycled SMO, LSM50, and LMO powder surfaces. (d) XPS Mn 2p and (e) ex situ XANES Mn K-edge spectra acquired on reduced and reoxidized (CDS) SMO, LSM50, and LMO powders.

This also indicates that CDS reactions cause disintegration of the LSM structure by CO_2 poisoning and C deposition. Surface carbon concentration (%) on the LSM samples during reduction, and CO_2- and H_2O-splitting reactions is shown in Figure 6c. Evidently, carbon deposition is lower during MPO−WS cycles when compared to MPO and MPO−CDS reactions. In addition, the surface carbon content decreased with La addition, which indicates that La contributes to impeding methane cracking and CO_2 poisoning. Interestingly, the surface carbon content on reduced SMO is lower than those on LSM25 and LSM50, which may be due to oxidation of the surface carbon species. High concentrations of oxygen species in the vacancy region (Figure 8a) and formation of 7.7% of the Mn_2O_3 phase are the possible explanations for this phenomenon.

A visual description of phase segregation in LSM samples after 10 consecutive MPO−CDS cycles is presented in Figure 7a,c,f. The blue region represents manganese on top of the strontium agglomerate (shown in red). Similarly, rodlike Sr-rich particles are observed on the particle aggregates, while the yellow, purple, and pink colors correspond to the coexisting Sr, Mn, La, and O elements in the LSM after cycling of LSM powders. Variable elemental peak intensities in EDS spectra confirm the different concentrations of Sr, Mn, and La at various points of the samples analyzed after cycling, as shown in Figure 7b,d,f.

Similar STEM maps are obtained on LSM samples after MPO−WS cycles. MnO particles are observed in SMO and LSM25, while high concentrations of the LSM phase indicate the perovskite structure recovery upon reoxidation by H_2O, Figure 7g,I,k. EDS spectra of SMO and LSM25 after WS cycles show different elemental concentrations at different regions of a sample (Figure 7h,j,l). The STEM maps of samples after MPO−CDS and MPO−WS cycles are in good agreement with the XRD results.

XPS and XANES analyses on reduced and reoxidized LSM powders provide critical insights into the electronic changes that occurred at surface and bulk levels. Figure 8a,b represents the O 1s region of the XPS spectra obtained on SMO, LSM50, and LMO powder surfaces after reduction and reoxidation reactions. Clearly, addition of La results in a broader lattice oxygen (OI) peak when compared to pure SMO and LMO samples. An increase in surface-adsorbed oxygen species (OIII) in reduced LMO powder surfaces is observed, which relates to surface oxygen-exchange activities. Reoxidation of LMO results in a decline in lattice oxygen species, and an intense peak for surface-adsorbed oxygen is observed. This may be due to lower oxygen exchange between LMO particles and CO_2, which results in lower CO production yields, as discussed in the section on thermochemical performance. In addition, the Sr concentration also plays a critical role in surface oxygen concentration. XPS data is utilized to estimate the oxygen concentration on LSM powder surfaces, as shown in Figure 8c. Apparently, an increase in the Sr content results in a higher concentration of surface oxygen species when compared to La-rich LSM structures. SMO powders possess the highest surface oxygen species during reduction and oxidation reactions, followed by LSM50 and LMO. This explains the low lattice oxygen peak in LMO after cycling. It is also observed that the Sr concentration is increased after CO_2-splitting reactions and is higher than that of H_2O-splitting reactions. This refers to higher redox activity by Sr at the SMO surface during CO_2-splitting reactions than that of H_2O-splitting reactions.

Deconvoluted XPS spectra of Mn 2p for SMO, LSM50, and LMO perovskite structures are shown in Figure 8d. Clearly, a satellite peak for MnO is observed in SMO and LSM50 samples, which confirms the XRD findings of structural disintegration after reduction and oxidation reactions. A shift toward lower binding energies is observed in the SMO sample after the reoxidation reaction, which also refers to oxygen depletion and lower oxidation states for manganese. In contrast, LMO showed a higher energy shift after the reoxidation reaction, while no considerable intensities for the satellite MnO peak are observed after cycling.

Changes in the Mn oxidation state are also investigated by XANES and EXAFS analyses after reduction and reoxidation reactions. The XANES spectra for the Mn K-edge are shown in Figure 8e and changes in oxidation states along with energy shifts for the Mn K-edge are presented in Table SI-3. The Mn K-edge shifts to lower energies i.e., 6544.6 eV in pure SMO and 6552.5 eV in LMO, after the MPO reaction, which corresponds to the creation of oxygen vacancies in the lattice. Oxidation states of LSM samples were calculated by comparing the experimental energy data with the standard data of Mn metal, MnO, Mn_2O_3, MnO_2, and Mn_3O_4, Table SI-3 and Figure SI-3. The oxidation states of SMO and LSM25 drastically decreased to 1.7 and 1.5, respectively, while only 0.3 cationic charge is removed from LMO after reduction. This confirms the high concentration of the MnO phase in pure SMO and LSM25 compared to LMO.

LSM samples underwent a certain degree of sintering during MPO−CDS and MPO−WS cycles. Fusion of small particles into agglomerates is observed in SMO, while an organized layer of individual particles can be seen in La-rich LSM structures, as shown in Figure 9. Particle sizes of SMO powders increased up to 400 nm ± 26 and 1 μm ± 200 nm during MPO−CDS and MPO−WS cycles, respectively. Addition of La showed suppressed particle size growth during cycling. With 25% La, particles sintered to sizes up to 289 nm ± 19 and 320 nm ± 15 during CDS and WS cycles, respectively. LMO samples consist of a particle network with average particle sizes

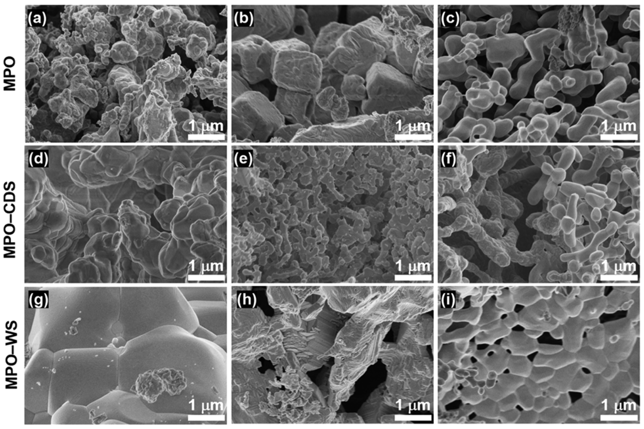

Figure 9. Morphological analysis of LSM powders after redox cycling: FESEM micrographs after cycling (a), (d), and (g) SMO, (b), (e), and (h) LSM50 and (c), (f), and (i) LMO samples. Particle growth and sintering are dominant in Sr-rich samples, while ordered individual particles are observed in pure LMO powders.

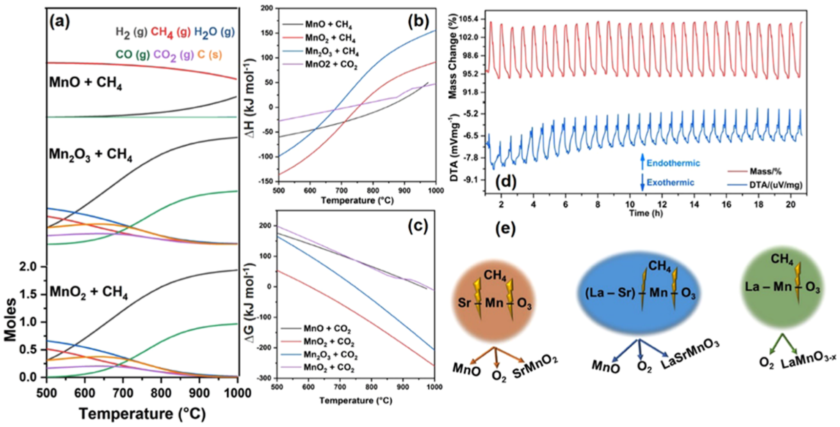

Figure 10. Mechanistic analysis for redox cycles: (a) products of the methane partial oxidation reaction by MnO, Mn_2O_3, and MnO_2. No activity for CO production is indicative of MnO participation in the MPO reaction. (b) Enthalpy and (c) Gibbs free energy of MPO and CDS reactions by different oxides of manganese. (d) TGA–DTA analysis for mass change and DTA measurements during 30 consecutive MPO–CDS redox cycles on the LSM25 sample. (e) Proposed mechanism of methane action on M–Mn and Mn–O bonds with and without lanthanum and its effect on the resulting products.

of 269 nm ± 17 and 342 nm ± 11 after MPO–CDS and MPO–WS cycling, respectively.

The morphological and surface features played a key role in the solid-to-gas transfer and agglomeration significantly affects the specific surface of powders. The BET analysis revealed that the as-prepared LSM25 powders have the highest specific surface area (SSA) of 11.56 m^2 g^{-1}, followed by SMO and LSM50. The SSA of LSM25 powders decreased by 35% after 10 consecutive MPO–CDS cycles, while a decline of 21, 55, and 71% in SSA was observed in the pure SMO, LSM50, and pure LMO powders, respectively, after cycling. The change in the surface area of powders was greater during the MPO–WS cycling, which aligns with the FESEM images shown in Figure 9g–i, where large particles in pure SMO, submicron agglomerates in LSM50, and a closed network of particles in the pure LMO powders were observed. This also aligns with the low thermochemical performance of LSM powders during MPO–WS cycling as compared to that in MPO–CDS cycling.

4. DISCUSSION AND FUTURE PERSPECTIVE

Manganese mono-oxide (MnO) is the byproduct of structural disintegration of LSM during redox cycling and does not contribute to either reduction or oxidation reactions. Figure 10a represents the reaction products of different oxide species of manganese with CH_4. Evidently, the MPO reaction by MnO does not result in any syngas product, except for H_2, which is produced due to the thermal cracking of methane after 900 °C. In contrast, MnO_2 and Mn_2O_3 actively reform methane at temperatures as low as 650 °C, producing considerable amounts of CO and H_2. The enthalpy of the reaction is higher for MnO_2 and Mn_2O_3 than that for MnO, which is in line with the published findings of the redox activity of pure manganese oxides (Figure 10b,c).[13] However, the structural configuration of perovskites enhances the redox activity by improving the oxygen-exchange capacity of manganese oxides, as Mn (B-site cation) is the active cation in oxygen exchange. This can only be achieved if structural stability is achieved to avoid the formation of the MnO phase, where La addition plays a key role in protecting the LSM structure from breakage.

TGA–DTA analysis for up to 30 consecutive cycles is performed on LSM25 to study the energy and mass losses during MPO–CDS redox cycles. Stable mass change profiles are observed during reduction and oxidation reactions (Figure 10d). A maximum of 10.5% mass change is achieved during the redox cycles. The enthalpy of reaction increases after three cycles to 10 cycles, which decreases and stabilizes afterward. The change in enthalpy may be due to the formation of the MnO phase in the LSM structure, which stabilizes when the MnO saturation level is achieved. The schematic illustration in Figure 10e explains the effect of La on the formation of the MnO phase and how it protects the Sr/La–Mn bond from being broken. Large concentrations of oxygen vacancies in La-rich LSM result in strong La–Mn/La–Sr–Mn bonds and weaken the Mn–O bond, which is opposite in Sr-rich LSM materials. This results in easy oxygen removal during the methane partial oxidation reaction. In contrast, the strong reducing power of CH_4 easily weakens the Sr–Mn bond and causes structural breakage.

The results of XANES and XPS studies about the change in Mn oxidation states are the key indicators of the involvement of Mn in redox activities. However, the formation of MnO appears to be unavoidable in stoichiometric reductions of the LSM structure. Addition of La to the lattice lowers the overall oxidation state of Mn, which results in a stronger Mn–O–(La/Sr) bond. This protects the LSM structure from breaking under the harsh reducing atmosphere of CH_4 and promotes nonstoichiometric reduction. The results of syngas production rates support this argument; the addition of La beyond 50% results in lower syngas rates and yields when compared to Sr-rich LSM samples. However, LMO produced considerable yields of syngas, while LSM25 and LSM50 are the best LSM structures for producing the highest syngas yields. In addition, 25 and 50% La addition materials also significantly lower MnO formation, and a considerable improvement in LSM structural regeneration is observed after reoxidation.

5. CONCLUSIONS

Strontium manganite perovskites with variable lanthanum concentrations (0, 25, 50, 75, and 100%) are studied for dry and steam chemical looping reforming of methane. The role of lanthanum in structural and phase stabilities in terms of phase disintegration and regeneration was the focus of this study. In addition, the effect of MnO formation on synthesis gas production rates and yields was also investigated. Incorporation of lanthanum resulted in lower manganese oxidation states in as-prepared LSM structures when compared to pure SMO. Lanthanum addition also prevented structural disintegration and promoted nonstoichiometric redox reaction mechanisms. Stoichiometric reduction of LSM structures results in structural breakage, which is unavoidable with high strontium concentrations. Syngas production yields are improved by 57 and 35% with 25 and 50% lanthanum, respectively, when compared to those of pure $SrMnO_3$ and $LaMnO_3$ perovskites. However, more than 50% lanthanum content shifts the redox behavior from stoichiometric to nonstoichiometric and lowers the overall syngas yields. In conclusion, this structural study provides insights into the redox behavior with respect to the structural changes in LSM perovskite oxides with the help of advanced characterization techniques.

■ ASSOCIATED CONTENT

Supporting Information

The Supporting Information is available free of charge at https://pubs.acs.org/doi/10.1021/acscatal.0c02439.

> Data on phase quantification and oxidation states of materials; EDS maps and spectra; and fitting curve for XANES analysis; Phases in pristine LSM powders, quantified by Rietveld refinement method applied on XRD patterns (Table S1-1); chemical analysis of pristine SMO sample: (a) gray scale and (b) colored overlay STEM−EDS map image of pristine SMO sample showing distribution of Sr (red) and Mn (blue); (c) STEM−EDS spectra acquired on pristine SMO sample (Figure S1-1) (PDF)

■ AUTHOR INFORMATION

Corresponding Authors

Wojciech Lipiński − *Research School of Electrical, Energy and Materials Engineering, The Australian National University, Canberra, ACT 2601, Australia;* orcid.org/0000-0001-5478-6887; Phone: +61 2 612 57896; Email: wojciech.lipinski@anu.edu.au

Adrian Lowe − *Research School of Electrical, Energy and Materials Engineering, The Australian National University, Canberra, ACT 2601, Australia;* orcid.org/0000-0001-7641-7724; Phone: +61 2 612 54881; Email: adrian.lowe@anu.edu.au

Authors

Asim Riaz − *Research School of Electrical, Energy and Materials Engineering, The Australian National University, Canberra, ACT 2601, Australia;* orcid.org/0000-0003-4903-2444

Takuya Tsuzuki − *Research School of Electrical, Energy and Materials Engineering, The Australian National University, Canberra, ACT 2601, Australia;* orcid.org/0000-0002-2002-3758

Felipe Kremer − *Centre for Advanced Microscopy, The Australian National University, Canberra, ACT 2601, Australia*

Suchinda Sattayaporn − *Synchrotron Light Research Institute (Public Organization), Muang District, Nakhon Ratchasima 30000, Thailand*

Muhammad Umair Ali − *Department of Materials Science and Engineering, College of Engineering, Peking University, Beijing 100871, China;* orcid.org/0000-0003-4115-0702

Complete contact information is available at: https://pubs.acs.org/10.1021/acscatal.0c02439

Notes

The authors declare no competing financial interest.

■ ACKNOWLEDGMENTS

This project was supported by the Australian Research Council (ARC Future Fellowship FT140101213 by W. Lipiński). This study used the facilities, with scientific and technical assistance, of the Centre of Advanced Microscopy at the Australian National University. We are grateful to Colin Carvolth and Kevin Carvolth for their assistance with setting up the IR furnace experiments.

■ REFERENCES

(1) Carrillo, A. J.; Bork, A. H.; Moser, T.; Sediva, E.; Hood, Z. D.; Rupp, J. L. M. Modifying La0.6Sr0.4MnO3 Perovskites with Cr Incorporation for Fast Isothermal CO2-Splitting Kinetics in Solar-Driven Thermochemical Cycles. *Adv. Energy Mater.* **2019**, *9*, No. 1803886.

(2) Bader, R.; Lipiński, W. Solar Thermal Processing. In *Advances in Concentrating Solar Thermal Research and Technology*; Blanco, M. J.; Santigosa, L. R., Eds.; Woodhead Publishing: Amsterdam, 2017; pp 403−459.

(3) Furler, P.; Scheffe, J. R.; Steinfeld, A. Syngas Production by Simultaneous Splitting of H_2O and CO_2 via Ceria Redox Reactions in a High-Temperature Solar Reactor. *Energy Environ. Sci.* **2012**, *5*, 6098−6103.

(4) Muhich, C. L.; Ehrhart, B. D.; Al-Shankiti, I.; Ward, B. J.; Musgrave, C. B.; Weimer, A. W. A Review and Perspective of Efficient Hydrogen Generation via Solar Thermal Water Splitting. *Wiley Interdiscip. Rev.: Energy Environ.* **2016**, *5*, 261−287.

(5) Marxer, D.; Furler, P.; Takacs, M.; Steinfeld, A. Solar Thermochemical Splitting of CO_2 into Separate Streams of CO and O_2 with High Selectivity, Stability, Conversion, and Efficiency. *Energy Environ. Sci.* **2017**, *10*, 1142−1149.

(6) Chueh, W. C.; Falter, C.; Abbott, M.; Scipio, D.; Furler, P.; Haile, S. M.; Steinfeld, A. High-Flux Solar-Driven Thermochemical Dissociation of CO_2 and H_2O Using Nonstoichiometric Ceria. *Science* **2010**, *330*, 1797−1801.

(7) Carrillo, R. J.; Scheffe, J. R. Advances and Trends in Redox Materials for Solar Thermochemical Fuel Production. *Sol. Energy* **2017**, *156*, 3−20.

(8) Huang, C.; Wu, J.; Chen, Y. T.; Tian, M.; Rykov, A. I.; Hou, B.; Lin, J.; Chang, C. R.; Pan, X.; Wang, J.; Wang, A.; Wang, X. In Situ Encapsulation of Iron(0) for Solar Thermochemical Syngas Production over Iron-Based Perovskite Material. *Commun. Chem.* **2018**, *1*, 2−11.

(9) Kodama, T.; Ohtake, H.; Matsumoto, S.; Aoki, A.; Shimizu, T.; Kitayama, Y. Thermochemical Methane Reforming Using a Reactive WO_3/W Redox System. *Energy* **2000**, *25*, 411−425.

(10) Lu, C.; Li, K.; Wang, H.; Zhu, X.; Wei, Y.; Zheng, M.; Zeng, C. Chemical Looping Reforming of Methane Using Magnetite as Oxygen Carrier: Structure Evolution and Reduction Kinetics. *Appl. Energy* **2018**, *211*, 1−14.

(11) Kodama, T.; Shimizu, T.; Satoh, T.; Shimizu, K.-I. Stepwise Production of CO-Rich Syngas and Hydrogen via Methane Reforming by a WO_3-Redox Catalyst. *Sol. Energy* **2003**, *28*, 1055−1068.

(12) Krenzke, P. T.; Fosheim, J. R.; Zheng, J.; Davidson, J. H. Synthesis Gas Production via the Solar Partial Oxidation of Methane-Ceria Redox Cycle: Conversion, Selectivity, and Efficiency. *Int. J. Hydrogen Energy* **2016**, *41*, 12799−12811.

(13) Gao, X.; Liu, G.; Zhu, Y.; Kreider, P.; Bayon, A.; Gengenbach, T.; Lu, T.; Liu, Y.; Hinkley, J.; Lipiński, W.; Tricoli, A. Earth-Abundant Transition Metal Oxides with Extraordinary Reversible

Oxygen Exchange Capacity for Efficient Thermochemical Synthesis of Solar Fuels. *Nano Energy* **2018**, *50*, 347−358.

(14) Riaz, A.; Kreider, P.; Kremer, F.; Tabassum, H.; Yeoh, J. S.; Lipiński, W.; Lowe, A. Electrospun Manganese-Based Perovskites as Efficient Oxygen Exchange Redox Materials for Improved Solar Thermochemical CO_2 Splitting. *ACS Appl. Energy Mater.* **2019**, *2*, 2494−2505.

(15) Welte, M.; Warren, K.; Scheffe, J. R.; Steinfeld, A. Combined Ceria Reduction and Methane Reforming in a Solar-Driven Particle-Transport Reactor. *Ind. Eng. Chem. Res.* **2017**, *56*, 10300−10308.

(16) Gibbons, W. T.; Venstrom, L. J.; De Smith, R. M.; Davidson, J. H.; Jackson, G. S. Ceria-Based Electrospun Fibers for Renewable Fuel Production via Two-Step Thermal Redox Cycles for Carbon Dioxide Splitting. *Phys. Chem. Chem. Phys.* **2014**, *16*, 14271−14280.

(17) Allendorf, M. D.; Diver, R. B.; Siegel, N. P.; Miller, J. E. Two-Step Water Splitting Using Mixed-Metal Ferrites: Thermodynamic Analysis and Characterization of Synthesized Materials. *Energy Fuels* **2008**, *22*, 4115−4124.

(18) Sahoo, T. R.; Armandi, M.; Arletti, R.; Piumetti, M.; Bensaid, S.; Manzoli, M.; Panda, S. R.; Bonelli, B. Pure and Fe-Doped CeO_2 nanoparticles Obtained by Microwave Assisted Combustion Synthesis: Physico-Chemical Properties Ruling Their Catalytic Activity towards CO Oxidation and Soot Combustion. *Appl. Catal., B* **2017**, *211*, 31−45.

(19) Kang, K. S.; Kim, C. H.; Cho, W. C.; Bae, K. K.; Woo, S. W.; Park, C. S. Reduction Characteristics of $CuFe_2O_4$ and Fe_3O_4 by Methane; $CuFe_2O_4$ as an Oxidant for Two-Step Thermochemical Methane Reforming. *Int. J. Hydrogen Energy* **2008**, *33*, 4560−4568.

(20) Kodama, T.; Kondoh, Y.; Yamamoto, R.; Andou, H.; Satou, N. Thermochemical Hydrogen Production by a Redox System of ZrO_2-Supported Co(II)-Ferrite. *Sol. Energy* **2005**, *78*, 623−631.

(21) Kodama, T.; Gokon, N.; Yamamoto, R. Thermochemical Two-Step Water Splitting by ZrO_2-Supported $Ni_xFe_{3-x}O_4$ for Solar Hydrogen Production. *Sol. Energy* **2008**, *82*, 73−79.

(22) Zheng, Y.; Zhu, X.; Wang, H.; Li, K.; Wang, Y.; Wei, Y. Characteristic of Macroporous CeO_2-ZrO_2 oxygen Carrier for Chemical-Looping Steam Methane Reforming. *J. Rare Earths* **2014**, *32*, 482−848.

(23) Cha, K. S.; Kim, H. S.; Yoo, B. K.; Lee, Y. S.; Kang, K. S.; Park, C. S.; Kim, Y. H. Reaction Characteristics of Two-Step Methane Reforming over a Cu-Ferrite/Ce-ZrO_2 Medium. *Int. J. Hydrogen Energy* **2009**, *34*, 1801−1808.

(24) Dong, W.-S.; Roh, H.-S.; Jun, K.-W.; Park, S.-E.; Oh, Y.-S. Methane Reforming over Ni/Ce-ZrO_2 Catalysts: Effect of Nickel Content. *Appl. Catal., A* **2002**, *226*, 63−72.

(25) Zhao, Z.; Uddi, M.; Tsvetkov, N.; Yildiz, B.; Ghoniem, A. F. Redox Kinetics and Nonstoichiometry of $Ce_{0.5}Zr_{0.5}O_{2-\delta}$ for Water Splitting and Hydrogen Production. *J. Phys. Chem. C* **2017**, *121*, 11055−11068.

(26) Kaneko, H.; Miura, T.; Ishihara, H.; Taku, S.; Yokoyama, T.; Nakajima, H.; Tamaura, Y. Reactive Ceramics of CeO_2-MO_x (M=Mn, Fe, Ni, Cu) for H_2 generation by Two-Step Water Splitting Using Concentrated Solar Thermal Energy. *Energy* **2007**, *32*, 656−663.

(27) Singh, P.; Hegde, M. S. $Ce_{0.67}Cr_{0.33}O_{2.11}$: A New Low-Temperature O_2 evolution Material and H_2 generation Catalyst by Thermochemical Splitting of Water. *Chem. Mater.* **2010**, *22*, 762−768.

(28) Tang, X.; Li, Y.; Huang, X.; Xu, Y.; Zhu, H.; Wang, J.; Shen, W. MnO_x-CeO_2 mixed Oxide Catalysts for Complete Oxidation of Formaldehyde: Effect of Preparation Method and Calcination Temperature. *Appl. Catal., B* **2006**, *62*, 265−273.

(29) Francis, T. M.; Lichty, P. R.; Weimer, A. W. Manganese Oxide Dissociation Kinetics for the Mn_2O_3 thermochemical Water-Splitting Cycle. Part 1: Experimental. *Chem. Eng. Sci.* **2010**, *65*, 3709−3717.

(30) Hong, F.; Yue, B.; Hirao, N.; Liu, Z.; Chen, B. Significant Improvement in Mn_2O_3 Transition Metal Oxide Electrical Conductivity via High Pressure. *Sci. Rep.* **2017**, *7*, No. 44078.

(31) Gao, X.; Bernardo, I.; Di; Kreider, P. B.; Tran-phu, T.; Cai, X.; Wang, N.; Lipton-duffin, J.; Bayon, A.; Lipi, W.; Tricoli, A. Lattice Expansion in Optimally-Doped Manganese Oxide: An Effective Structural Parameter for Enhanced Thermochemical Water Splitting. *ACS Catal.* **2019**, *9*, 9880−9890.

(32) Gao, X.; Vidal, A.; Bayon, A.; Bader, R.; Hinkley, J.; Lipiński, W.; Tricoli, A. Efficient Ceria Nanostructures for Enhanced Solar Fuel Production via High-Temperature Thermochemical Redox Cycles. *J. Mater. Chem. A* **2016**, *4*, 9614−9624.

(33) Riaz, A.; Ali, M. U.; Lipiński, W.; Lowe, A. Enhanced Oxygen Exchange Capacity in Nano-Structured Vanadia−Ceria Multi-Phase Oxygen Carriers for Solar Thermal Fuel Production. *J. Mater. Chem. A* **2019**, *7*, 27347−27360.

(34) Le Gal, A.; Abanades, S. Dopant Incorporation in Ceria for Enhanced Water-Splitting Activity during Solar Thermochemical Hydrogen Generation. *J. Phys. Chem. C* **2012**, *116*, 13516−13523.

(35) Riaz, A.; Ali, M. U.; Enge, T. G.; Tsuzuki, T.; Lowe, A.; Lipiński, W. Concentration-Dependent Solar Thermochemical CO_2 /H_2O Splitting Performance by Vanadia−Ceria Multiphase Metal Oxide Systems. *Research* **2020**, *2020*, No. 3049534.

(36) Zhao, K.; Li, L.; Zheng, A.; Huang, Z.; He, F.; Shen, Y.; Wei, G.; Li, H.; Zhao, Z. Synergistic Improvements in Stability and Performance of the Double Perovskite-Type Oxides $La_{2-x}Sr_xFeCoO_6$ for Chemical Looping Steam Methane Reforming. *Appl. Energy* **2017**, *197*, 393−404.

(37) Neal, L.; Shafiefarhood, A.; Li, F. Effect of Core and Shell Compositions on MeO_x@$La_ySr_{1-Y}FeO_3$ Core-Shell Redox Catalysts for Chemical Looping Reforming of Methane. *Appl. Energy* **2015**, *157*, 391−398.

(38) Ding, H.; Xu, Y.; Luo, C.; Wang, Q.; Shen, C.; Xu, J.; Zhang, L. A Novel Composite Perovskite-Based Material for Chemical-Looping Steam Methane Reforming to Hydrogen and Syngas. *Energy Convers. Manage.* **2018**, *171*, 12−19.

(39) Li, L.; Song, Y.; Jiang, B.; Wang, K.; Zhang, Q. A Novel Oxygen Carrier for Chemical Looping Reforming: $LaNiO_3$ Perovskite Supported on Montmorillonite. *Energy* **2017**, *131*, 58−66.

(40) Gokon, N.; Yawata, T.; Bellan, S.; Kodama, T.; Cho, H. S. Thermochemical Behavior of Perovskite Oxides Based on La_xSr_{1-x}(Mn, Fe, Co)$O_{3-\Delta}$ and $Ba_ySr_{1-Y}CoO_{3-\Delta}$ Redox System for Thermochemical Energy Storage at High Temperatures. *Energy* **2019**, *171*, 971−980.

(41) Jiang, Q.; Zhang, H.; Cao, Y.; Hong, H.; Jin, H. Solar Hydrogen Production via Perovskite-Based Chemical-Looping Steam Methane Reforming. *Energy Convers. Manage.* **2019**, *187*, 523−536.

(42) Carrillo, R. J.; Scheffe, J. R. Beyond Ceria: Theoretical Investigation of Isothermal and Near- Isothermal Redox Cycling of Perovskites for Solar Thermochemical Fuel Production. *Energy Fuels* **2019**, *33*, 12871−12884.

(43) Hua, X.; Fan, Y.; Wang, Y.; Fu, T.; Fowler, G. D.; Zhao, D.; Wang, W. The Behaviour of Multiple Reaction Fronts during Iron (III) Oxide Reduction in a Non-Steady State Packed Bed for Chemical Looping Water Splitting. *Appl. Energy* **2017**, *193*, 96−111.

(44) Yang, E.; Noh, Y. S.; Hong, G. H.; Moon, D. J. Combined Steam and CO_2 reforming of Methane over $La_{1-x}Sr_xNiO_3$ Perovskite Oxides. *Catal. Today* **2018**, *299*, 242−250.

(45) Barcellos, D. R.; Coury, F. G.; Emery, A.; Sanders, M.; Tong, J.; McDaniel, A.; Wolverton, C.; Kaufman, M.; O'Hayre, R. Phase Identification of the Layered Perovskite $Ce_xSr_{2-X}MnO_4$ and Application for Solar Thermochemical Water Splitting. *Inorg. Chem.* **2019**, *58*, 7705−7714.

(46) Shafiefarhood, A.; Stewart, A.; Li, F. Iron-Containing Mixed-Oxide Composites as Oxygen Carriers for Chemical Looping with Oxygen Uncoupling (CLOU). *Fuel* **2015**, *139*, 1−10.

(47) Galinsky, N.; Sendi, M.; Bowers, L.; Li, F. $CaMn_{1-x}B_xO_{3-\delta}$ (B = Al, V, Fe, Co, and Ni) Perovskite Based Oxygen Carriers for Chemical Looping with Oxygen Uncoupling (CLOU). *Appl. Energy* **2016**, *174*, 80−87.

(48) Nune, S. K.; Rama, K. S.; Dirisala, V. R.; Chavali, M. Y. Electrospinning of Collagen Nanofiber Scaffolds for Tissue Repair and Regeneration. In *Nanostructures for Novel Therapy*; Elsevier, 2017; pp 281−311.

(49) Agarwal, S.; Wendorff, J. H.; Greiner, A. Use of Electrospinning Technique for Biomedical Applications. *Polymer* **2008**, *49*, 5603−5621.

(50) Shen, Y.; Zhao, K.; He, F.; Li, H. The Structure-Reactivity Relationships of Using Three-Dimensionally Ordered Macroporous $LaFe_{1-x}Ni_xO_3$ Perovskites for Chemical-Looping Steam Methane Reforming. *J. Energy Inst.* **2019**, *92*, 239−246.

(51) Biesinger, M. C.; Payne, B. P.; Grosvenor, A. P.; Lau, L. W. M.; Gerson, A. R.; Smart, R. S. C. Resolving Surface Chemical States in XPS Analysis of First Row Transition Metals, Oxides and Hydroxides: Cr, Mn, Fe, Co and Ni. *Appl. Surf. Sci.* **2011**, *257*, 2717−2730.

(52) Wu, Q. H.; Liu, M.; Jaegermann, W. X-Ray Photoelectron Spectroscopy of $La_{0.5}Sr_{0.5}MnO_3$. *Mater. Lett.* **2005**, *59*, 1980−1983.

(53) Krenzke, P. T.; Fosheim, J. R.; Davidson, J. H. Solar Fuels via Chemical-Looping Reforming. *Sol. Energy* **2017**, *156*, 48−72.